Journal of Materials Chemistry C

ROYAL SOCIETY OF CHEMISTRY

PAPER

View Article Online
View Journal | View Issue

Cite this: J. Mater. Chem. C, 2025, 13, 20114

Multifunctional PANI–TiO_2–Fe_3O_4@attapulgite 3D composites for synergistic microwave absorption and corrosion protection

Kai Xu, Pei Liu, Yinxu Ni, Qingqing Gao, Jin Chen, Shuai Yin, Zixuan Ding, Guohui Tang, Changtian Zhu and Fenghua Liu*

Electromagnetic (EM) pollution has emerged as a pressing concern, driving the demand for high-performance microwave absorbing materials. In this work, attapulgite (ATP) was employed as a natural, porous scaffold for the *in situ* integration of amorphous TiO_2, Fe_3O_4, and polyaniline (PANI), constructing a multifunctional composite with tailored dielectric and magnetic properties. The TiO_2 and PANI coatings not only induced strong interfacial and conduction polarization but also formed a continuous 3D conductive network, enabling efficient energy dissipation. Benefiting from the magneto–electric synergy among PANI, TiO_2, and Fe_3O_4, the composite exhibited multiple loss mechanisms and excellent impedance matching. As a result, a minimum reflection loss of −56.24 dB was achieved at 11.63 GHz (2.9 mm thickness), with an ultra-wide effective absorption bandwidth of 8.1 GHz. More importantly, by integrating 3D printing with metamaterial-inspired design, the absorption range was successfully extended into the low-frequency region (4–6 GHz), while simultaneously enhancing structural integrity and corrosion resistance. This study offers a scalable strategy for designing lightweight, corrosion-resistant microwave absorbers by combining hierarchical conductive frameworks with multifunctional components, opening new avenues for next-generation EM shielding and stealth technologies.

Received 19th June 2025,
Accepted 19th August 2025

DOI: 10.1039/d5tc02365c

rsc.li/materials-c

1. Introduction

With the extensive application of electromagnetic wave technology, electromagnetic interference (EMI) and electromagnetic wave pollution have emerged as increasingly critical issues, directing materials science research towards the development of high-performance electromagnetic wave absorbing materials.[1–3] These materials are designed to effectively mitigate mutual interference among electronic devices and shield human health from the potential risks associated with electromagnetic radiation.[4] In recent years, researchers have successfully engineered a range of high-performance electromagnetic wave absorbing materials by refining material composition and structural design.[5–7] By harnessing synergistic effects between dielectric and magnetic losses, these materials demonstrate exceptional electromagnetic wave absorption capabilities across a broad frequency spectrum,[8–10] thereby paving the way for innovative research and applications in the domain of electromagnetic wave absorption.[11]

Among them, M_2FeC MAX phase materials with multi-principal elements (M = Ti, V, Nb, Ta, and Zr) exhibit significant potential in the field of electromagnetic wave absorption owing to their unique composition and structure.[12] By fine-tuning the element composition and structure, these materials can effectively achieve a synergistic effect between dielectric and magnetic losses, thereby enabling efficient absorption of electromagnetic waves across a wide frequency range. On the other hand, NiAl-layered[8] double hydroxide/graphene composites significantly enhance electromagnetic wave absorption capabilities by harnessing interfacial polarization effects, while also demonstrating excellent corrosion resistance.[13]

Furthermore, the application of core–shell engineering techniques has opened up new avenues for the development of electromagnetic wave absorbing materials. For instance, Palygorskite@Fe_3O_4@polyperfluoroalkylsilane[14] not only possesses superoleophobic properties and magnetic liquid marble characteristics but also shows broad application prospects in the field of electromagnetic wave absorption. Similarly, hierarchical porous carbon Fe_3O_4@Fe composites[15] designed through loofah sponge carbonization and Fe_3O_4@black TiO_{2-x}[16] heterostructures engineered with disordered structures to augment dielectric polarization offer innovative approaches for achieving high-performance electromagnetic wave absorption.

State Key Laboratory of Advanced Marine Materials, Ningbo Institute of Materials Technology & Engineering, Chinese Academy of Sciences, Ningbo, 315201, P. R. China. E-mail: lfh@nimte.ac.cn

Absorption materials demonstrate efficient electromagnetic wave absorption across a wide frequency spectrum by strategically manipulating their compositional and structural design, thereby achieving effective synergies between dielectric and magnetic losses.[17–20] However, these materials often impose specific requirements on their intended application environments. Under complex real-world conditions, maintaining both excellent absorption performance and corrosion resistance poses a significant challenge.[21–23] Consequently, research into corrosion-resistant absorption materials with superior performance is both necessary and important.[24]

In this work, one-dimensional nanometer attapulgite (ATP) was employed as a framework to create a cost-effective,[25] environmentally friendly,[26] high aspect ratio,[27] and structurally stable core–shell structure (PANI–TiO_2–Fe–ATP). This composite material exhibited remarkable microwave absorption properties, achieving a minimum reflection loss (RL_{min}) of −56.24 dB at 11.63 GHz for a PANI–TiO_2–Fe–ATP coating with 20 wt% loading. Furthermore, the effective absorption bandwidth (EAB) spanned 8.10 GHz at a coating thickness of 2.6 mm. These impressive microwave absorption characteristics can be primarily attributed to the magneto–electric effect, interfacial polarization, multiple losses, and good impedance matching, which are facilitated by the synergistic interaction between the PANI–TiO_2–Fe nanoparticle shells and ATP nanorods. Additionally, comprehensive evaluations, including salt spray tests, Tafel polarization curves, Nyquist plots, impedance moduli, and phase angle plots, demonstrate that the PANI–TiO_2–Fe–ATP coating exhibits exceptional corrosion resistance and electromagnetic wave absorption performance. Overall, this work provides a cost-effective, environmentally friendly, and highly efficient approach for constructing one-dimensional nano-network composites tailored for microwave absorption and corrosion resistance.

2. Results and discussion

2.1. Preparation of PANI–TiO_2–Fe–ATP

ATP possesses a large number of active groups, such as Si–OH. During coprecipitation, Fe ions will replace Si–OH to form Si–OFe groups.[28] The addition of $NH_3{\cdot}H_2O$ solution provides an alkaline environment conducive to the growth of Fe_3O_4 NPs. According to crystallographic principles, crystals tend to grow on surfaces with the minimum potential barrier. Therefore, Fe_3O_4 will preferentially grow along the Si–OFe groups. Consequently, Fe_3O_4 NPs will anchor on the surface of ATP.

In this work, tetrabutyl titanate was selected as the Ti source for growing an amorphous TiO_2 shell on the surface of ATP. Tetrabutyl titanate readily reacted with water to form a TiO_2 sol, and providing an alkaline environment accelerated this reaction. Here, $NH_3{\cdot}H_2O$ solutions were used to create a weak alkaline environment, allowing for controlled reaction rates.[29] The thickness of the TiO_2 shell was influenced by the amount of $NH_3{\cdot}H_2O$ solution added, with higher alkalinity resulting in a thicker TiO_2 shell.[30] Fe–ATP has been prepared as in the previous step, eddy current loss occurs when magnetic materials generate eddy currents and undergo energy conversion in response to changes in an external magnetic field. However, significant eddy current loss presents a considerable challenge, particularly in high-conductivity materials such as metals, as it reduces the maximum incident depth of microwaves and inhibits their absorption. One effective solution to this issue is the precise control of the microscopic dimensions of magnetic materials to either enhance or suppress eddy current loss. Extensive research has shown that when the size of iron oxide (Fe_3O_4) particles decreases, the influence of eddy current loss on electromagnetic waves is correspondingly reduced. When the particle size falls within the range of 80–200 nm, the effect of eddy current loss can be decrease to an acceptable level.[4,29,30]

This work uses the traditional *in situ* growth method for the preparation of a PANI shell. In an acidic environment, ATP composites activate Si–OH groups, assigning a negative charge to the ATP.[16,31–33] Aniline synthesizes PANI through the action of APS, resulting in positively charged PANI.[34,35] The positively charged PANI and negatively charged ATP composites then combine through electrostatic self-assembly.[35,36] ATP powder exhibits a strong agglomeration effect under dry conditions. However, interestingly, in homogeneous solutions, ATP rods experience a stronger van der Waals force than agglomeration force, leading to the formation of a 3D structure.[37] During the preparation of Fe–ATP and TiO_2–Fe–ATP, the Fe_3O_4 and amorphous TiO_2 shells do not possess sufficient thickness to stabilize the 3D structure of ATP. However, PANI has a lower density compared to Fe and Ti materials. An ice bath facilitates stable and complete growth of PANI.[38] During the *in situ* growth of PANI, hydrochloric acid reacts with a portion of Fe_3O_4, weakening the magnetism of the composites. PANI has sufficient volume to cover and stabilize the 3D structure of ATP, ensuring that the final composites maintain their 3D structure after being removed from the homogeneous solution.

2.2. Microstructure and chemical composition

Fig. 1 and Fig. S1 present the microstructure and elemental distribution of the samples. As shown in Fig. 1(a) and Fig. S1(d), the ATP exhibits a rod-like shape structure. Most ATP rods have lengths in the range of 300 to 400 nm and diameters of 30 to 60 nm. ATP is rich in chemical groups such as –OH and –Mg, which can enhance its combination rate with other groups. The ATP appears as regular rods with a smooth surface and exhibits a weak agglomeration effect, forming channels. Fig. 2(b) shows Fe_3O_4 nanoparticles covering the ATP rods as tiny particles. It is evident from Fig. 2(b) that Fe_3O_4 has a better distribution. Fe–ATP also presents a coralloid-like structure. As shown in Fig. 1(c), TiO_2 is coated onto the Fe–PANI surface in the form of a thin layer. The elemental content from EDS clearly confirms the presence of Ti, with its mass fraction being comparable to that of Al in ATP. The presence of ATP is well supported by SEM, TEM, and XRD analyses. After PANI is coated onto the TiO_2–Fe–ATP composites, the overall morphology undergoes a significant transformation. The PANI layer without Fe_3O_4 exhibits a granular surface structure. However, the introduction of

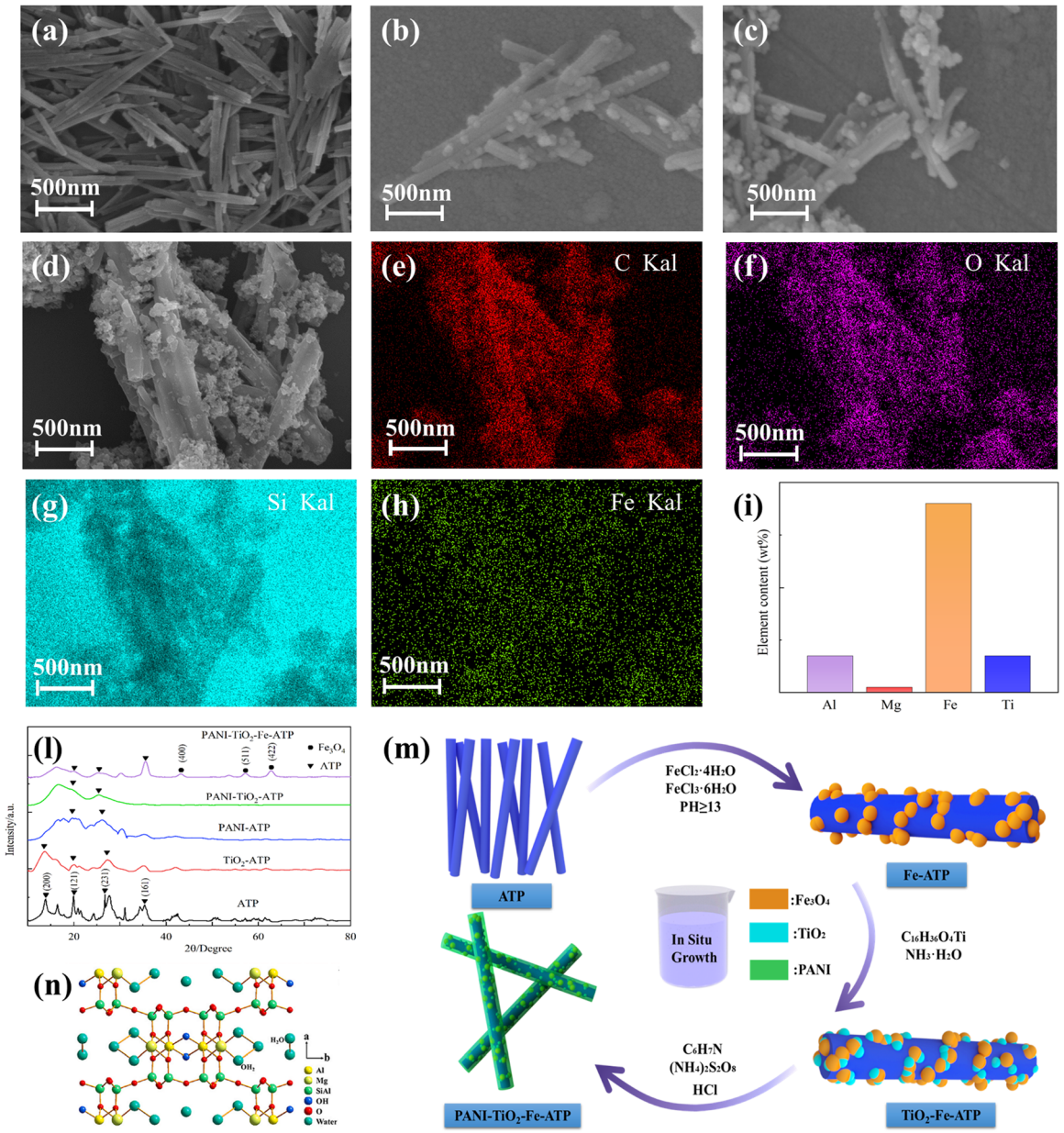

Fig. 1 SEM images of (a) ATP, (b) Fe–ATP, (c) TiO_2–Fe–ATP, and (d) PANI–TiO_2–Fe–ATP. Elemental distribution profiles corresponding to PANI–TiO_2–Fe–ATP of (e), (f), (g), (h) and (i) elemental contents of Al, Mg, Fe, and Ti. (l) XRD patterns. (m) Illustration of the synthesis process of PANI–TiO_2–Fe–ATP. (n) Crystal structure of ATP.

large-sized Fe_3O_4 particles promotes the formation of a more uniform PANI coating. As a result, in the PANI–TiO_2–Fe–ATP composite, the microstructure is primarily characterized by ATP loaded with spherical particles. This leads to a localized aggregation of the spherical particles, contributing to the morphological changes observed in Fig. 1(d). As shown in Fig. S1(f), TiO_2 and Fe_3O_4 particles exhibit a certain degree of aggregation, but they remain anchored onto the ATP surface. The PANI coating exhibits a thickness ranging from 19 to 22 nm, with a noticeable increase in thickness around larger particles.

Fig. S1(g)–(i) confirm the presence of C, O, Ti, and Mg elements. In the full survey spectrum, distinct signals corresponding to carbon and oxygen are observed. As evidenced in Fig. S1(h), the oxygen peak at 530 eV is attributed to Ti–O bonding. Furthermore, the Ti 2p spectrum in Fig. S1(i) exhibits characteristic spin–orbit doublets at 559 eV (Ti $2p_{1/2}$) and 566 eV (Ti $2p_{3/2}$).[39] Although the Fe signal near 720 eV in XPS is significantly attenuated due to dissolution in dilute hydrochloric acid, its residual presence is corroborated by XRD diffraction patterns. The peak at 180 eV originates from Si in ATP, while the N 1s peak at 400 eV confirms the successful incorporation of PANI. Notably, the O 1s component associated with Ti–O bonds and adsorbed water species enhances electromagnetic wave attenuation through strengthened dipole polarization.[40] Collectively, these analytical results demonstrate

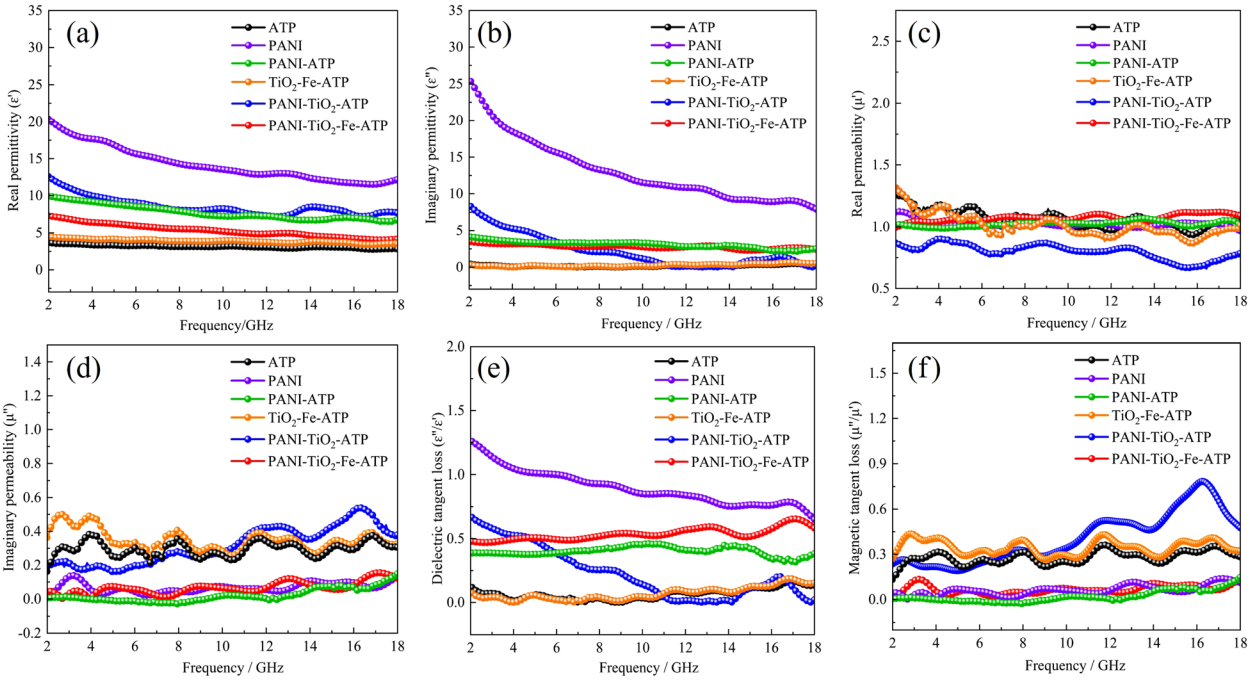

Fig. 2 Dielectric properties of the samples of (a) ε', (b) ε'', (c) μ', (d) μ'', (e) tan δ_e, and (f) tan δ_u.

the successful synthesis of the PANI–TiO_2–Fe–ATP composite material.

Fig. 1(l) presents the XRD patterns of (a) ATP, PANI–ATP, PANI–TiO_2–ATP, and PANI–TiO_2–Fe–ATP, while Fig. S1(b) shows the elemental distribution of Fe, Ti, and Al. Pure ATP exhibits distinct diffraction peaks at $2\theta = 13.9^\circ$, 16.5°, 19.9°, 28°, and 35.6°, corresponding to the (2 0 0), (−1 3 0), (1 2 1), (2 3 1), and (1 6 1) planes, respectively, which are indexed to ATP. PANI displays prominent peaks at $2\theta = 18^\circ$ and 26°, corresponding to the (0 2 0) and (2 0 0) planes, indexed to PANI. In the composites, the low-intensity peak at 19.9° corresponds to ATP, and another low-intensity peak at 26° belongs to PANI. These results confirm the successful combination of ATP and PANI. When amorphous titanium is deposited on the ATP surface, the diffraction peaks change to a halo peak characteristic of the amorphous phase. This indicates that amorphous titanium has successfully bonded with ATP and significantly affects its conduction ability. Additionally, the prominent peaks appear at 34.6°, 56°, and 62.3°, indexed to ICDD No. 01-071-6336,[41] corresponding to Fe_3O_4. This confirms the successful binding of ferric oxide to the ATP surface. According to Fig. S1(b) and (c), the Fe element accounts for only a small proportion of the mass. The Fe element is present and distributed within the rod structure, indicating the presence of TiO_2, albeit at a very low content.

In attapulgite, Mg frequently occupies active sites that can exchange with other metal elements, creating a conducive environment for the attachment of additional metals. Analyzing the elemental proportions, we observe that the mass fraction of Mg in the composite material is relatively low. This indicates that, during the synthesis of the composite, Fe and Ti elements underwent extensive ion exchange. However, because Fe elements exchanged with Mg first, they occupied a larger number of active sites on the attapulgite surface. Consequently, the subsequent growth of Ti elements was limited to a few remaining active sites, making it challenging to detect Ti elements in the element distribution map. Despite this, the presence of amorphous TiO_2 is clearly confirmed by XRD analysis.

2.3. EM wave absorption mechanism

Fig. 2 shows the dielectric properties of ATP, PANI, PANI–ATP, TiO_2–Fe–ATP, PANI–TiO_2–ATP, and PANI–TiO_2–Fe–ATP samples. The previous work demonstrated that the 20 wt% filler loading exhibited optimal wave-absorption performance while producing more homogeneous and stable test specimens. Therefore, in this work, all samples were prepared with a fixed solid content of 20 wt%. According to the transmission line theory, the reflection loss (RL) and impedance are calculated as shown below:[42,43]

$$Z = \left|\frac{Z_{in}}{Z_0}\right| = \sqrt{\frac{\mu_r}{\varepsilon_r}}\tanh\left[j\left(\frac{2\pi fd}{c}\right)\sqrt{\mu_r\varepsilon_r}\right] \quad (1)$$

$$RL = 20\log\left|\frac{Z_{in} - Z_0}{Z_{in} + Z_0}\right| \quad (2)$$

where Z_{in} and d are the input impedance and the thickness of the absorber, Z_0 is the impedance of free space, ε_r and μ_r are the permittivity and permeability of the absorber and c is the speed of light.

Fig. 2 presents the electromagnetic parameters of pure ATP, PANI, PANI–ATP, TiO_2–Fe–ATP, PANI–TiO_2–ATP, and PANI–TiO_2–Fe–ATP. As shown in Fig. 2(a), the real permittivity (ε') and imaginary permittivity (ε'') are displayed, with pure PANI

exhibiting higher values compared to the other materials. Additionally, PANI-based composites demonstrate higher ε' values than pure ATP and TiO_2–Fe–ATP composites across the entire frequency range of 2 to 18 GHz. Fig. 3(b) illustrates that PANI–TiO_2–Fe–ATP has the highest ε'' among all samples, while the other composites show comparable values in numerical analysis, indicating that PANI–TiO_2–Fe–ATP possesses strong dielectric loss capacity. The discontinuous distribution of Fe_3O_4 particles of different sizes and amorphous TiO_2 enhances interfacial polarization and dipole polarization. It is worth noting that the values of ε' and ε'' for all materials decrease significantly with increasing frequency.

In addition, Fig. 2(c) and (d) present the magnetic characteristics of the samples. Notably, PANI–TiO_2–ATP exhibits the lowest values of μ' among all the samples. Although XRD patterns confirm the growth of Fe_3O_4 on the ATP surface, the addition of Fe_3O_4 results in only a slight change in the magnetic loss curves, indicating that the materials retain weak magnetic loss ability. Fe_3O_4 NPs generate a weak electromagnetic field, contributing to enhanced EM absorption. Based on the results of magnetic loss and dielectric loss tangent, it is evident that the dielectric loss is the primary mechanism for microwave absorption in these samples. Fig. 2(e) displays the tangent value of dielectric loss. PANI has the highest $\varepsilon''/\varepsilon'$ value among all samples, demonstrating the strongest dielectric loss capacity, as also shown in Fig. 2(b).

A strong dielectric introduces multiple loss mechanisms, including interfacial polarization, conductivity loss, and dipole polarization. However, a high $\varepsilon''/\varepsilon'$ value may lead to poor impedance matching. In this study, globular Fe_3O_4 and amorphous TiO_2 were sequentially grown on the ATP surface. The growth of amorphous TiO_2 on Fe–ATP helps to reduce dielectric values, thereby improving impedance matching. PANI and PANI composite materials exhibit excellent conductivity and primarily contribute to conductivity losses. The conductivity significantly improves when PANI is added to the composites. The rod-like ATP provides abundant pores and functional groups, creating a favorable environment for the positive growth of TiO_2 and Fe_3O_4, resulting in multiple polarizations within the materials.

2.4. The Cole–Cole curve

Debye theory is an important parameter of the EM wave. Debye theory could analyze the polarization relaxation and explained

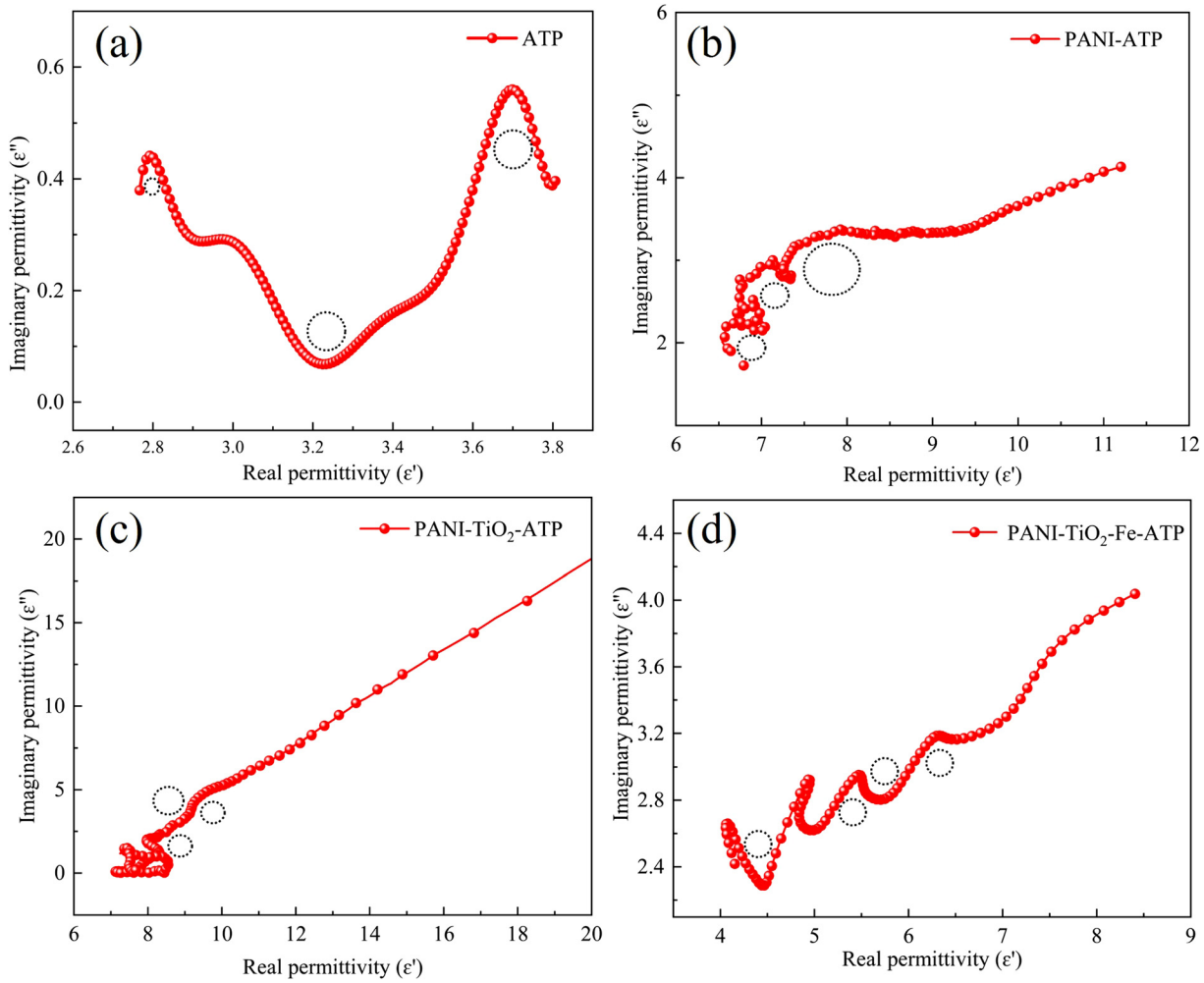

Fig. 3 Cole–Cole circles of (a) ATP, (b) PANI–ATP, (c) PANI–TiO_2–ATP, and (d) PANI–TiO_2–Fe–ATP.

between ε' and ε'' as shown below:[19,33]

$$\varepsilon' = \varepsilon_\infty + \frac{\varepsilon_s - \varepsilon_\infty}{1 + \omega^2\tau^2} \quad (3)$$

$$\varepsilon'' = \frac{\varepsilon_s - \varepsilon_\infty}{1 + \omega^2\tau^2}\omega\tau + \frac{\sigma}{\omega\varepsilon_0} \quad (4)$$

$$\left(\varepsilon' - \frac{\varepsilon_s + \varepsilon_\infty}{2}\right) + (\varepsilon'')^2 = \left(\frac{\varepsilon_s - \varepsilon_\infty}{2}\right)^2 \quad (5)$$

where ε_s and ε_s are the static permittivity and relative dielectric permittivity at the high frequency limit. ω and τ represent the angular frequency and polarization relaxation time. σ represents the alternating current conductivity.

Debye theory is represented as a Cole–Cole circle to elucidate the relaxation processes of ATP, PANI–ATP, PANI–TiO_2–ATP, and PANI–TiO_2–Fe–ATP. As shown in Fig. 4(a), pure ATP exhibits at least three large radii and variable curves, indicating abundant interfacial polarization. This can be attributed to the numerous natural pores and functional groups on the ATP surface. In Fig. 4(b), PANI–ATP displays two small circles and a big circle, suggesting strong dielectric loss. The polymer PANI forms a shell around the rod-like ATP, enhancing its permittivity and providing a multiple interface effect when exposed to microwaves. As illustrated in Fig. 4(c) and (d), PANI–TiO_2–ATP and PANI–TiO_2–Fe–ATP demonstrate significant radius changes in their curves, indicating a substantial increase in both interfacial and dipole polarizations.

Notably, PANI–TiO_2–Fe–ATP has a larger radius compared to the other materials. According to Fig. 3(c), amorphous TiO_2 has a strong influence on ATP, particularly by altering its conductivity. The globular Fe_3O_4 particles, formed *via* the coprecipitation mechanism, have larger sizes (30 to 50 nm) than the amorphous TiO_2 particles (10 to 20 nm). The presence of different elements and multiple particle sizes leads to increased interactions, further enhancing interfacial and dipole polarizations.

Analysis of the dielectric parameters from the electromagnetic measurements reveals an overall decreasing trend in the complex permittivity during the composite formation process, indicating that the conductive loss dominates the attenuation mechanism. This is further corroborated by the Cole–Cole plots, where the curves exhibit a combination of quasi-linear segments and semicircular arcs. The linear portion corresponds to conductive loss, while the semicircular feature arises from polarization–relaxation processes.

As the composite forms, the polarization–relaxation contribution increases significantly. Previous studies suggest that this enhancement is associated with the incorporation of TiO_2, which increases the specific surface area and introduces abundant pores, thereby strengthening interfacial polarization.[44] Additionally, variations in the dielectric loss tangent ($\tan\delta_e = \varepsilon''/\varepsilon'$) exhibit corresponding peak shifts, further confirming the enhanced polarization effects. These modifications contribute to improved electromagnetic wave (EMW) absorption performance.[45]

2.5. EM wave absorption mechanism

Fig. 4 shows the microwave absorption properties of ATP, Fe–ATP, PANI–ATP, TiO_2–Fe–ATP, and PANI–TiO_2–Fe–ATP. It presents the RL (reflection loss) curves and three-dimensional profiles of the composites at various thicknesses. As illustrated in Fig. 4(a) to 5(f), pure ATP exhibits a matching thickness of 2.6 mm at 17.2 GHz within the Ku-band (12 to 18 GHz) and achieves a minimum RL of −11.93 dB. The optimal matching thickness for Fe–ATP is also 2.6 mm, reaching −8.6 dB. The

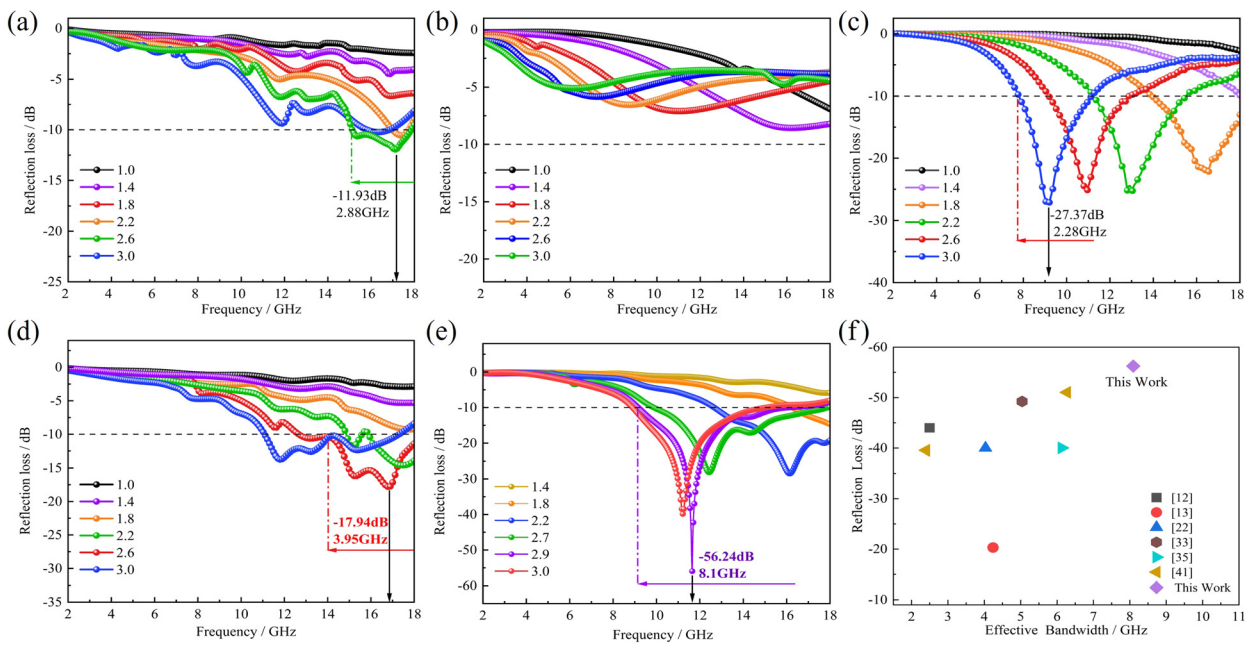

Fig. 4 Electromagnetic wave absorption performance. Reflection loss (RL) curves of (a) ATP, (b) Fe–ATP, (c) PANI–ATP, (d) TiO_2–Fe–ATP, and (e) PANI–TiO_2–Fe–ATP. (f) Reflection loss and effective bandwidth performance comparison.[12,13,22,33,35]

TiO_2–Fe–ATP composites achieve −17.94 dB at a 2.6 mm thickness, with an effective bandwidth of 4.11 GHz. The incorporation of amorphous TiO_2 adjusts the impedance to a suitable level and increases the material's surface area. Compared to pure ATP, both Fe–ATP and Fe–TiO_2–ATP exhibit better minimum reflection loss values. PANI–ATP has a matching thickness of 3.0 mm and reaches a minimum RL of −27.37 dB at 9.18 GHz, with a bandwidth of 2.28 GHz. The PANI shell significantly increases both ε' (real part of permittivity) and ε'' (imaginary part of permittivity). However, an excessive increase in dielectric capability can lead to impedance imbalance and a decrease in reflection loss. The reflection loss of PANI–ATP indicates that the addition of PANI achieves a better RL value than the simple combination of each individual substance, as it enhances conductivity and provides more discontinuous areas. As shown in Fig. 4(e), the PANI–TiO_2–Fe–ATP composites have a matching thickness of 2.6 mm and reach −56.24 dB at 11.63 GHz. The addition of Fe_3O_4 slightly improves the microwave absorption performance. Interestingly, the introduction of magnetic loss widens the composite's bandwidth from 4.11 to 8.1 GHz. The different sizes of the two nanoparticles (NPs) not only increase the discontinuous dispersion and interfacial polarization but also induce more dipole polarization. The 3D network structure provides more reflection, and the dual shell (TiO_2 and PANI) converts more electromagnetic waves into other forms of energy.

2.6. Impedance matching

Impedance matching is a very important factor for EM wave absorption. Strong EM wave absorption requires Z value to tend to 1 which will lead to high electromagnetic wave penetration. However, high attenuation constant (α) will reduce the residual EM wave. The expression for α is as follows:[22]

$$\alpha = \frac{\sqrt{2\mu'\varepsilon'}\pi f}{c}\sqrt{(\tan\delta\varepsilon\tan\delta\mu - 1) + \sqrt{(\tan\delta\varepsilon\tan\delta\mu - 1)^2 + (\tan\delta\varepsilon + \tan\delta\mu)^2}} \quad (6)$$

Fig. 5 presents the impedance matching curves and attenuation constant of ATP, Fe–ATP, TiO_2–Fe–ATP, PANI–ATP, and PANI–TiO_2–Fe–ATP. Regarding the frameworks, pure ATP possesses a natural nano-structure and abundant groups, but it exhibits poor impedance and reflection loss (as shown in Fig. 5a and 3a). Upon doping with Fe_3O_4 nanoparticles, the impedance matching shows a preliminary improvement due to the introduction of magnetic losses. The impedance matching ratio decreases significantly from 2 to 0.6, resulting in low μ' (real part of permeability) and high ε'' (imaginary part of permittivity). According to previous research, the incorporation of dielectric loss materials (such as TiO_2, PANI, and Pyy) further enhances the balance of impedance matching. In this work, amorphous TiO_2 coating and PANI were added as dual shells to improve impedance. As illustrated in Fig. 5(c), amorphous TiO_2 adjusts the balance between permittivity and permeability by reducing either permittivity or permeability, achieving an impedance matching ratio of 1.5. Amorphous TiO_2 also provides dipole polarization and a high attenuation constant.

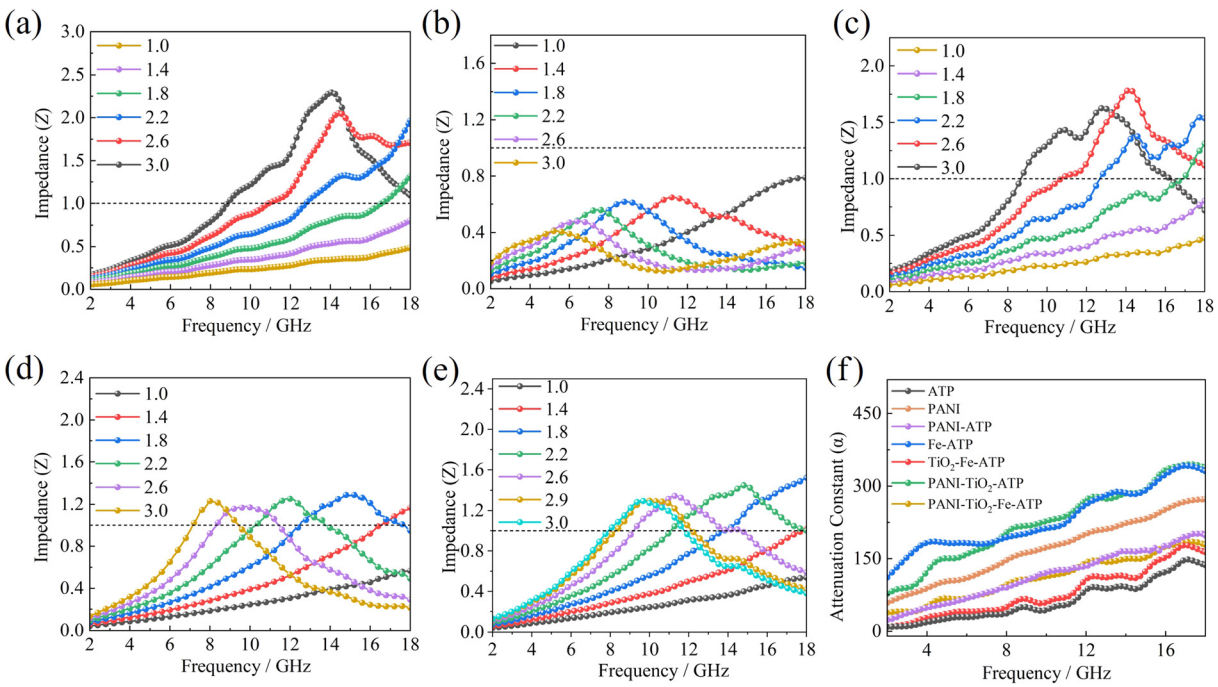

Fig. 5 Impedance match (Z) curves of (a) ATP, (b) Fe–ATP, (c) TiO_2–Fe–ATP, (d) PANI–ATP, and (e) PANI–TiO_2–Fe–ATP and their (f) attenuation constant (α).

Following the addition of PANI, the PANI–TiO_2–Fe–ATP composites exhibit even better impedance matching. PANI not only introduces conduction loss but also enhances the dispersion of the ATP framework, leading to the formation of a 3D structure.

Fig. S2 illustrates the multiple loss mechanisms in the composite material. The 1D rod-like ATP possesses natural nano-channels, which introduce defect polarization similar to that caused by oxygen vacancies. The incorporation of Fe_3O_4 nanoparticles introduces magnetic loss by generating a magnetic field around the particles. The cation exchange properties of ATP facilitates the aggregation of Fe_3O_4, leading to a more effective magnetic field distribution. The dielectric TiO_2, with its large surface area, not only balances the impedance matching but also provides dipole polarization and creates an uneven interface with Fe_3O_4.[3] Upon the addition of PANI to the composites, PANI and TiO_2 form a dual shell around ATP, resulting in an improved impedance match. PANI possesses good electrical conductivity, which enhances electron migration. In this work, PANI has connected the rod-like composites together to form a 3D nano-structure. This network provides more current paths and reflections, converting more electromagnetic waves into energy loss. In summary, PANI–TiO_2–Fe–ATP combines the advantages of individual materials to create a multi-effect microwave absorption mechanism.

The attenuation coefficient (α) analysis reveals that Fe–ATP exhibits the strongest electromagnetic wave (EMW) attenuation capability among the studied compositions. Although its impedance matching falls within a favorable range, ensuring efficient EMW penetration into the material, the overall reflection loss (RL) performance remains limited. Compared to pristine ATP, the Fe–ATP composite shows a low-frequency shift in the RL peak but no significant enhancement in RL intensity. This suggests that the Fe–ATP system lacks diversified loss mechanisms, and its single dominant attenuation pathway restricts further improvement in EMW absorption performance.[46]

To address this limitation, we introduced PANI and TiO_2 to enrich the loss mechanisms. While PANI alone tends to disrupt impedance matching, the synergistic incorporation of TiO_2 in this work effectively balances the impedance matching characteristics while maintaining robust attenuation capability. The resulting PANI–TiO_2–Fe–ATP composite achieves broadband and high-efficiency EMW absorption performance.

2.7. Microwave absorption of metamaterial absorbers

A gradient structure (L = 4, 5, 6, 7, 8, 9, and 10 and h = 2, 2.2, 2.4, 2.6, 2.8, 3.0) was designed to improve both the microwave reflection loss and effective bandwidth. Compared to pure composites, the gradient structure enhanced the effective

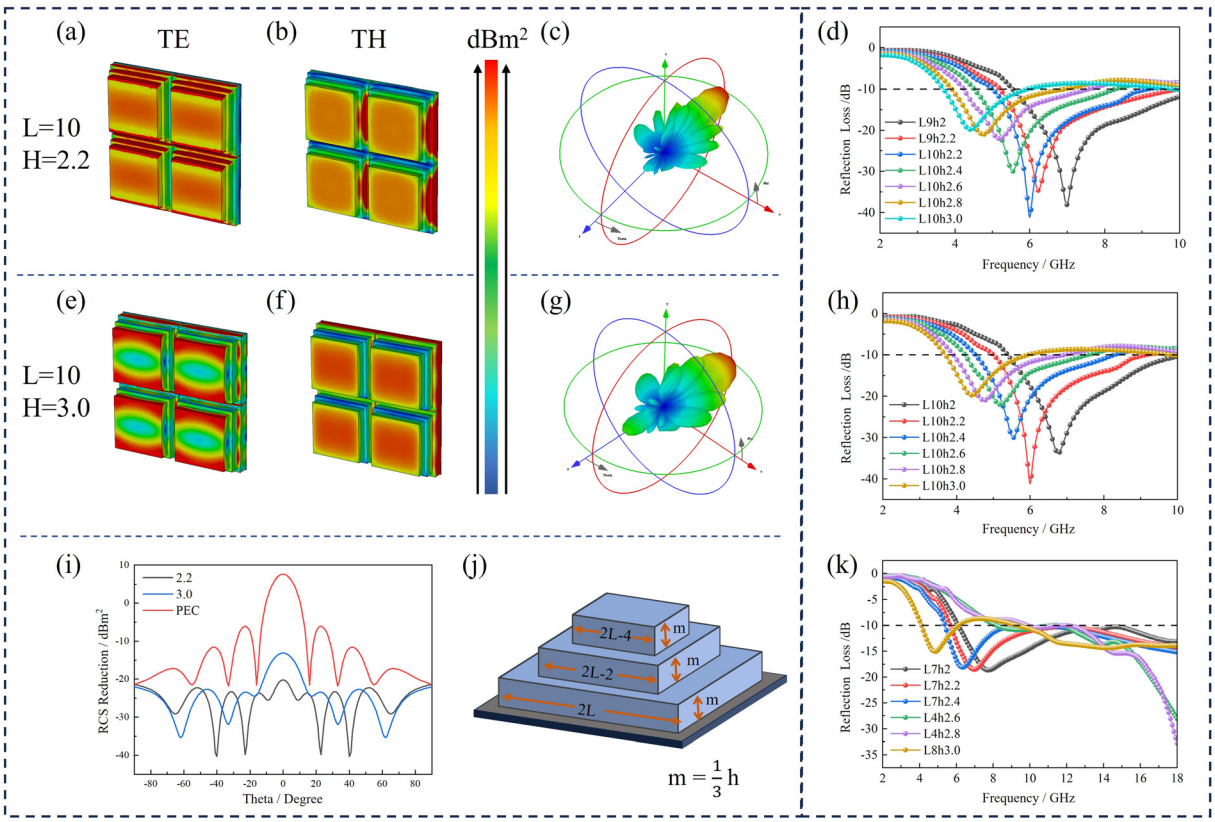

Fig. 6 (a) and (e) TE, (b) and (f) TH polarization, (c) and (g) 3D RCS absorption of L10 h2.2 and L10 h3.0. (i) RCS reduction and (j) gradient structure design. Microwave absorption performance under different structural parameters (h = 2, 2.2, 2.4, 2.6, 2.8, 3.0; L = 0, 1, 2, 3, 4, 5, 6, 7, 8, 9, 10). (d) Optimal parameters for the small-band. (h) Lowest frequency for each thickness. (k) Maximum effective bandwidth for each thickness under different size parameters.

bandwidth range from 8.1 to 12.62 GHz (Fig. 6) that covered C and Ku bands. As the thickness increased, the absorption peak shifted to a low frequency (Fig. S3). L10 h2.2 reach −42.56 dB at 5.99 GHz and L10 h3.0 have the lowest frequency at 3.68 GHz, covering a range from 3.68 to 6 GHz. As shown in Fig. 6(a), the electric and magnetic fields of the microwave absorber are concentrated at the edge of the gradient structure, indicating that the interference dominates at this frequency. Furthermore, the electric loss is predominant in the composites, as the electric field loss exceeds the magnetic field loss. According to Fig. S4, the gradient structure absorber maintains effective microwave absorption ability when the microwave degree changes from 0 to 60°.

The radar cross section (RCS) is used to simulate the far-field EM response, reflecting real-world conditions (Fig. 6(c), (g) and (i) and Fig. S5). In this work, a 180 × 180 mm coating was applied to a perfect electrical conductor (PEC) plate. The L10 h2.2 and L10 h3.0 samples exhibited good RCS reduction values of 28.44 dB m^2 and 20.65 dB m^2. The materials and structure demonstrated an excellent synergy effect in microwave absorption.[44] The 3D conduction network of PANI–TiO_2–Fe–ATP increases the ingress of EM waves, optimizing impedance matching and broadening the transmission path of EM waves, thereby enhancing attenuation capability. This 3D conduction network provides more interfacial polarization, which enhances conduction loss and helps convert microwave energy to thermal energy. At the macro scale, the gradient structure offers more reflection loss and provides flexibility to suit complex real environments by adjusting the parameters of the gradient structure. This allows for adjustments according to the required frequency, such as the 5G communication frequency band from 4 to 6 GHz. Additionally, the gradient structure facilitates edge diffraction and resonance among adjacent unit cells, introducing a new loss mechanism.

The trilayered trapezoidal structure shown in Fig. 6(j) demonstrates a sophisticated electromagnetic wave absorption mechanism through three distinct yet interconnected processes, as evidenced by Fig. 6(a)–(f). When electromagnetic waves first encounter the absorber surface, they undergo edge diffraction and interfacial polarization, where the conductive PANI network initiates preliminary absorption while directing energy concentration toward the peripheral regions, accounting for the observed enhanced energy dissipation at the material edges. This effect is further amplified by the oriented arrangement of ATP particles during fabrication, which becomes more pronounced under polarization fields and significantly influences the spatial distribution of energy dissipation.

As waves penetrate deeper into the material, the PANI–TiO_2–Fe–ATP composite engages multiple attenuation mechanisms. The heterogeneous interfaces between components generate substantial interfacial polarization, while the embedded ferrite particles interact strongly with incident radiation through dipole relaxation processes. These interactions produce pronounced damping effects that significantly enhance dipole polarization losses, as documented in ref. 47 and 48. Simultaneously, the incorporated TiO_2 nanoparticles contribute through their high surface area and porous structure, which promote multiple scattering events and additional interface polarization effects.

The final absorption stage occurs through structural interactions, where the strategically designed voids between adjacent trapezoidal units create conditions for multiple wave reflections. These geometric features not only prolong the electromagnetic wave propagation path within the material but also establish resonant cavity effects that further intensify energy dissipation. The combination of these three phases, such as surface interaction, bulk attenuation, and structural resonance, creates a comprehensive absorption system where each element works synergistically. The trapezoidal configuration specifically addresses impedance matching requirements through its gradual structural transitions while optimizing energy capture efficiency through its unique geometric design, ultimately resulting in superior broadband absorption performance.

2.8. Anticorrosion properties

In this work, the anti-corrosion properties of composite materials are demonstrated through Tafel curves. The composite film was coated onto conductive copper and then subjected to corrosion in NaCl solutions. Under stable open circuit conditions, the cathode and anode exhibit equal corrosion rates. When the circuit remains stable and open, the corrosion rates are manifested through corrosion parameters, namely the corrosion potential (E_{corr}) and corrosion current density (I_{corr}). Consequently, E_{corr} and I_{corr} are also utilized to characterize the corrosion rates.

Fig. 7 and Table 1 present the Tafel curves, Nyquist plots, impedance moduli, and phase angle plots of copper and copper coated with various materials. Among the five samples, uncoated copper exhibited a corrosion potential (E_{corr}) of 0.087 V and a corrosion current density (I_{corr}) value of 6.123×10^{-7} A cm^{-2}. After being coated with ATP coating, E_{corr} shifted to 0.150 V and I_{corr} increased to 5.333×10^{-5} A cm^{-2}. With the Fe–ATP coating, E_{corr} changed to 0.126 V and I_{corr} increased to 1.880×10^{-4} A cm^{-2}, indicating that both ATP and Fe–ATP coatings accelerated the corrosion of copper.[21] However, the addition of amorphous TiO_2 and a PANI shell reversed this trend. When coated with TiO_2–Fe–ATP coating, E_{corr} shifted to −0.067 V and I_{corr} decreased to 3.296×10^{-8} A cm^{-2}. For the copper with the PANI–TiO_2–Fe–ATP coating, E_{corr} changed to −0.083 V and I_{corr} reduced to 6.397×10^{-11} A cm^{-2}, demonstrating that both TiO_2–Fe–ATP and PANI–TiO_2–Fe–ATP coatings could protect copper from corrosion, with the PANI–TiO_2–Fe–ATP coating performing significantly better than the others. Based on previous research, it is reasonable to hypothesize that PANI initially prevents and weakens the corrosive substances, while amorphous TiO_2 provides a porous structure that further buffers the corrosive substances from reaching the metal. This mitigates the detrimental effects of Fe and ATP on corrosion resistance.

Fig. 7(b)–(d) present the Nyquist plots, impedance modulus curves, and phase angle plots, respectively. The outstanding anti-corrosion performance of the PANI–TiO_2–Fe–ATP coating

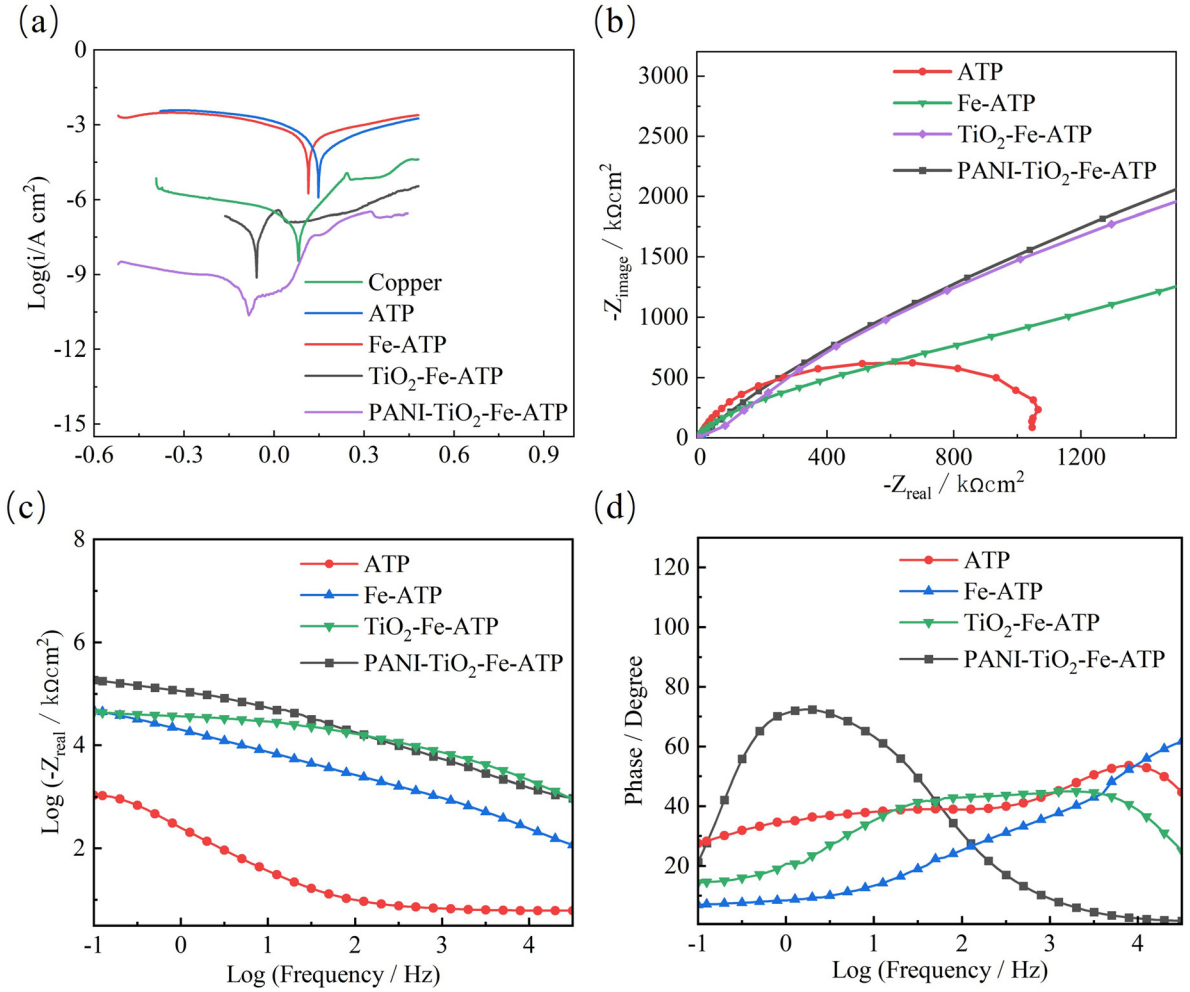

Fig. 7 (a) Tafel polarization curves of copper, ATP, Fe–ATP, TiO_2–Fe–ATP and PANI–TiO_2–Fe–ATP. (b) Nyquist plots, (c) impedance moduli and (d) phase angle plots of ATP, Fe–ATP, TiO_2–Fe–ATP and PANI–TiO_2–Fe–ATP.

Table 1 Electrochemical parameters obtained from the Tafel polarization curves of copper, ATP, Fe–ATP, TiO_2–Fe–ATP and PANI–TiO_2–Fe–ATP

Coatings	E_{corr}/V	I_{corr} (A cm^{-2})
Copper	0.087	6.123×10^{-7}
ATP	0.150	5.333×10^{-5}
Fe–ATP	0.126	1.880×10^{-4}
TiO_2–Fe–ATP	−0.067	3.296×10^{-8}
PANI–TiO_2–Fe–ATP	−0.083	6.397×10^{-11}

is evident from these three types of curves. For both copper and ATP, a distinct circle is observable at low frequencies in the Nyquist plots, indicating the occurrence of dissolution and pitting corrosion during the corrosion test. In contrast, the other coatings exhibit larger circles, which signify superior anti-corrosion performance. Both PANI–TiO_2–Fe–ATP and TiO_2–Fe–ATP demonstrate higher impedance moduli, with PANI–TiO_2–Fe–ATP showing a larger phase angle at low frequencies. This indicates that PANI–TiO_2–Fe–ATP possesses better corrosion resistance compared to the other material coatings. Furthermore, Fig. S6 displays the results of the salt spray test conducted on different coatings after 1000 hours. After this duration, both copper and Fe–ATP exhibited prominent outward erosion traces and extensive erosion spots at the X-shaped scratch. Conversely, TiO_2–Fe–ATP and PANI–TiO_2–Fe–ATP showed a significantly reduced tendency for outward corrosion after 1000 hours, with corrosion primarily confined to the X-shaped scratch. Furthermore, PANI–TiO_2–Fe–ATP demonstrated an even more concentrated corrosion pattern exclusively around the X-shaped scratch, highlighting a remarkable improvement in its overall corrosion resistance.

3. Conclusions

In summary, ATP has been effectively combined with PANI, amorphous TiO_2, and Fe_3O_4. PANI not only facilitates conduction polarization but also reinforces the 3D structure by acting as a bridge between the composite materials. The resulting PANI–TiO_2–Fe–ATP composite exhibits a minimum reflection loss value of −56.24 dB at 11.63 GHz with a thickness of 2.9 mm and achieves an effective bandwidth of 8.1 GHz. The materials and structure exhibited an excellent synergistic effect in

microwave absorption, covering a frequency range from 3.64 to 6 GHz, and achieved a remarkable RCS reduction value of 28.44 dB m^2. Importantly, the PANI–TiO_2–Fe–ATP coating demonstrates reduced self-corrosion tendencies, and its multi-shell, 3D conductive structure further enhances its anti-corrosion properties. Consequently, the PANI–TiO_2–Fe–ATP composite material emerges as a promising low-cost microwave absorber, combining both electrical and magnetic loss mechanisms.

4. Experimental

4.1. Materials

Attapulgite was provided by Lanzhou Institute of Chemical Physics, Chinese Academy of Sciences. Ammonium persulfate (APS), aniline and tetrabutyl titanate were purchased from Aladdin Chemical Reagent Co., Ltd. Aqueous ammonia (25–28%) and concentrated hydrochloric acid (33–36%) purchased from Sinopharm Chemical Reagent Co., Ltd. Ferric chloride hexahydrate ($FeCl_3·6H_2O$), and ferrous chloride ($FeCl_2·4H_2O$) were purchased from Aladdin Chemical Reagent Co., Ltd.

4.2. Materials preparation

4.2.1. Preparation of Fe–ATP. The starting material was prepared using a coprecipitation mechanism. Firstly, 1.0 g ATP, 5.0 g $FeCl_3·6H_2O$ and 5 g $FeCl_2·4H_2O$ were mixed with 200 mL of deionized water in a beaker. After stirring for 30 min, aqueous ammonia ($NH_3·H_2O$) was added until the solution reached a pH of 13 or higher, and the mixture was stirred for 24 h. The resulting sample was then dried at 60 °C for 10 h. This powder is referred to as Fe–ATP.

4.2.2. Preparation of TiO_2–Fe–ATP. Firstly, 1 g of ATP and 1.6 mL of aqueous ammonia ($NH_3·H_2O$) were added to 350 mL of absolute ethanol, and magnetic stirring for 15 min to ensure complete mixing. This solution was designated as solution A. Then, 5 mL of tetrabutyl titanate was rapidly added to 50 mL of absolute ethanol and magnetically stirred for 30 min to form solution B. Next, solution B was slowly dripped into solution A, and the mixture was magnetically stirred for 24 h. Under the action of $NH_3·H_2O$, the TiO_2 was gradually loaded onto the surface of ATP. Finally, the mixed solutions were centrifuged, washed with absolute ethanol, and dried at 100 °C for 10 h to obtain TiO_2–Fe–ATP.

4.2.3. Synthesis of PANI–TiO_2–Fe–ATP. ATP-dispersed TiO_2/PANI composites were prepared by polymerization. 1 g TiO_2–ATP powder and 5.79 g ammonium persulfate (APS) were added into 100 mL hydrochloric acid solution (HCl, 0.33 mol L^{-1}) in a 500 mL beaker and mechanically stirred for 10 min at 0–5 °C. Then 2.3 g aniline was slowly dropped into the beaker at 0–5 °C, the temperature was maintained and the mixture was mechanically stirred for 4 h. Finally, PANI–TiO_2–ATP composites were collected by vacuum filtration and washed with deionized water and absolute ethanol and dried at 100 °C for 10 h. Compounded materials were named PANI–TiO_2–Fe–ATP.

4.3. DLP printing process and parameters

The formulated photosensitive resin was loaded into the resin vat of a DLP 3D printer (Anycubic Photon Ultra, Shenzhen Zongwei Cube Technology Co., Ltd), and layer-by-layer fabrication was carried out based on a pre-designed 3D digital model. This spatially controlled polymerization enables the liquid resin to solidify in a patterned manner, building the final structure through successive layer stacking. To enhance interfacial bonding and prevent early-stage detachment, the initial exposure settings were systematically optimized to balance polymerization depth and interlayer cohesion. Specifically, a normal exposure time of 36 seconds was applied with a 2 second off time between layers. For the bottom layers, which serve as the foundation for structural integrity, an increased exposure time of 90 seconds was used for 5 initial layers. The layer thickness was maintained at 0.05 mm to achieve high-resolution feature formation and dimensional accuracy. Posting processing involved UV post-curing for 2 minutes using a combined curing and washing unit (Wash&Cure Plus, Shenzhen Zongwei Cube Technology Co., Ltd).

4.4. Performance testing and characterization methods

The microscopic morphology and element distribution were characterized using a field emission scanning electron microscope (FESEM, Hitachi Limited, S4800) and a transmission electron microscope (TEM, Tecnai F20). The crystal structure was analyzed using an X-ray diffractometer (XRD, Shimadzu, Lab-X XRD-6000). Reflection (UV-vis) studies were conducted using a PE Lambda 950 spectrophotometer. The electromagnetic parameters were measured using an Agilent E8363B network analyzer. Anticorrosion properties (Tafel polarization curves, Nyquist plots, impedance moduli and phase angle plots) were measured with Modu-Lab.

Author contributions

All authors contributed to the scientific discussion and manuscript preparation. Kai Xu: conceptualization, methodology, validation, data curation, writing – review and editing and writing – original draft; Pei Liu, Qingqing Gao, Yinxu Ni, and Shuai Yin: conceptualization, investigation, writing – review and editing and data curation; Changtian Zhu and Guohui Tang: data curation and validation; Jin Chen and Zixuan Ding: conceptualization, formal analysis, and supervision; Fenghua Liu: conceptualization, resources, project administration, supervision, funding acquisition, and writing – review and editing.

Conflicts of interest

There are no conflicts of interest to declare.

Data availability

The data that support the findings of this study are available from the corresponding author upon reasonable request.

Supplementary information is available. See DOI: https://doi.org/10.1039/d5tc02365c

Acknowledgements

This work was supported by the Key Research and Development Program of Ningbo (2023Z107) and the Special project of Gansu Regional Science and Technology Cooperation (20JR10QA579).

References

1 S. Wang, W. Lian, H. Ren, J. Ma, Y. Lin, T. Zhang and L. Kong, *New J. Chem.*, 2021, **45**, 2765–2774.
2 C. Jin, Z. Wu, C. Yang, L. Wang, R. Zhang, H. Xu and R. Che, *Chem. Eng. J.*, 2022, **433**, 133640–133650.
3 L. Huang, C. Chen, X. Huang, S. Ruan and Y. Zeng, *Composites, Part B*, 2019, **164**, 583–589.
4 X. Shi, Z. Liu, X. Li, W. You, Z. Shao and R. Che, *Chem. Eng. J.*, 2021, **419**, 130020–130030.
5 L. Li, B. Li, L. Fan, B. Mu, A. Wang and J. Zhang, *J. Mater. Chem. A*, 2016, **4**, 5859–5868.
6 H. Zhang, F. Yang, Q. Zhang, A. Hui and A. Wang, *ACS Appl. Bio Mater.*, 2022, **5**, 3960–3971.
7 G. Meng, X. Mu, L. Zhen, J. Hai, Z. Zhang, T. Hao, S. Lu, A. Wang and B. Wang, *Chem. Sci.*, 2022, **13**, 14141–14150.
8 M. Sun, C. Xu, J. Li, L. Xing, T. Zhou, F. Wu, Y. Shang and A. Xie, *Chem. Eng. J.*, 2020, **381**, 122615–122622.
9 P. Chen, S. He, Z. Zou, T. Wang, J. Hu, J. Tao, L. Yang and Y. Li, *Adv. Funct. Mater.*, 2025, 2506308–2506320.
10 Y. Liao, G. He and Y. Duan, *Chem. Eng. J.*, 2021, **425**, 130512–130530.
11 C. Wang, Y. Liu, Z. Jia, W. Zhao and G. Wu, *Nano-Micro Lett.*, 2022, **15**, 13–29.
12 B. Mu and A. Wang, *J. Environ. Chem. Eng.*, 2016, **4**, 1274–1294.
13 H. Wang, H. Ren, C. Jing. Li, Q. Zhou and F. Meng, *Compos. Sci. Technol.*, 2021, **204**, 108630–108640.
14 Q. Wang, B. Niu, Y. Han, Q. Zheng, L. Li and M. Cao, *Chem. Eng. J.*, 2023, **452**, 139042–139054.
15 F. Wu, M. Sun, W. Jiang, K. Zhang, A. Xie, Y. Wang and M. Wang, *J. Mater. Chem. C*, 2016, **4**, 82–88.
16 J. Ding, D. Huang, W. Wang, Q. Wang and A. Wang, *Int. J. Biol. Macromol.*, 2019, **122**, 684–694.
17 W. Wang and A. Wang, *Appl. Clay Sci.*, 2016, **119**, 18–30.
18 X. Wang, X. Chen, B. Wang, Q. He, J. Cao, Y. Zhu, K. Su, H. Yan, P. Sun, R. Li, J. Zhang and J. Shao, *Small*, 2025, 2412744.
19 Z. Wu, H. Cheng, C. Jin, B. Yang, C. Xu, K. Pei, H. Zhang, Z. Yang and R. Che, *Adv. Mater.*, 2022, **34**, e2107538.
20 Z. Cai, P. Sun, L. I. Ardhayanti, S. Islam, T. Tsugawa, K. Kuroiwa, Y. Sekine, S. Ida and S. Hayami, *J. Mater. Chem. A*, 2025, **13**, 6607–6619.
21 Z. Tong, Z. Liao, Y. Liu, M. Ma, Y. Bi, W. Huang, Y. Ma, M. Qiao and G. Wu, *Carbon*, 2021, **179**, 646–654.
22 G. Wu, Z. Jia, X. Zhou, G. Nie and H. Lv, *Composites, Part A*, 2020, **128**, 105687–105697.
23 R. Islam, H. Mudila, R. Chahal, A. Ohlan and A. Kumar, *J. Mater. Chem. A*, 2025, **13**, 14751.
24 C. Wen, H. Liu, L. Luo, Z. Cui, X. Li, J. Jin and B. Sa, *J. Mater. Chem. C*, 2024, **12**, 17037–17049.
25 S. Kim, S. Lee, Y. Zhang, S. Park and J. Gu, *Adv. Sci.*, 2023, **10**, 2303104.
26 M. Qin, L. Zhang and H. Wu, *Adv. Sci.*, 2022, **9**, e2105553.
27 P. Bhattacharya, S. Dhibar, M. K. Kundu, G. Hatui and C. Das, *Mater. Res. Bull.*, 2015, **66**, 200–212.
28 X. Zhou, Z. Jia, A. Feng, J. Kou, H. Cao, X. Liu and G. Wu, *Composites, Part B*, 2020, **192**, 107980–107992.
29 P. Liu, Y. Li, H. Xu, L. Shi, J. Kong, X. Lv, J. Zhang and R. Che, *ACS Nano*, 2024, **18**, 560–570.
30 W. Li, Y. Liu, F. Guo, Y. Du and Y. Chen, *Appl. Surf. Sci.*, 2021, **562**, 150212–150224.
31 F. Wu, M. Sun, C. Chen, T. Zhou, Y. Xia, A. Xie and Y. Shang, *ACS Sustainable Chem. Eng.*, 2018, **7**, 2100–2106.
32 J. Liu, J. Zhong, Z. Chen, J. Mao, J. Liu, Z. Zhang, X. Li and S. Ren, *Appl. Surf. Sci.*, 2021, **565**, 150398–150408.
33 J. Yan, Q. Zheng, S. Wang, Y. Tian, W. Gong, F. Gao, J. Qiu, L. Li, S. Yang and M. Cao, *Adv. Mater.*, 2023, **35**, e2300015.
34 Z. Du, S. Shen, X. Su, Y. Zhuang, M. Chen, X. Zhang, Z. Lin, L. Yu, P. Zhou, M. Wu, X. Lyu and Z. Zou, *Adv. Mater.*, 2025, 2502328.
35 G. Tian, W. Wang, L. Zong, Y. Kang and A. Wang, *RSC Adv.*, 2016, **6**, 41696–41706.
36 W. Xie, J. Wang, K. Shang, H. Chen, A. Tang, M. Wu, X. Cui and H. Yang, *Mater. Adv.*, 2022, **3**, 6799–6808.
37 W. Li, J. Yang, Z. Wu, J. Wang, B. Li, S. Feng, Y. Deng, F. Zhang and D. Zhao, *J. Am. Chem. Soc.*, 2012, **134**, 11864–11867.
38 Z. Li, F. Liu, G. Xu, J. Zhang and C. Chu, *Colloid Polym. Sci.*, 2014, **292**, 3327–3335.
39 S. Shao, S. Xing, K. Bi, C. Guo, Y. Tang, L. Wu, Z. Wang, J. Liu and F. Wang, *Small*, 2025, **21**, 2502349.
40 Y. Tang, S. Shao, C. Guo, K. Bi, H. Wang, T. Zhao, J. Liu and F. Wang, *Carbon*, 2024, **228**, 119314.
41 V. Lalan and S. Ganesanpotti, *Chem. Eng. J.*, 2023, **461**, 141857.
42 T. Song, C. Xia, Y. Ding, S. Liu, B. Chen, Z. Feng, T. Yang and Q. Li, *Corros. Sci.*, 2022, **208**, 110685–110703.
43 L. Gai, L. Guo, Q. An, Z. Xiao, S. Zhai and Z. Li, *Microporous Mesoporous Mater.*, 2019, **288**, 109584–109597.
44 V. Lalan and S. Ganesanpotti, *J. Mater. Chem. C*, 2022, **10**, 969–982.
45 S. Shao, C. Guo, H. Wang, S. Wang, T. Zhao, Y. Tang, J. Liu and F. Wang, *Chem. Eng. J.*, 2024, **488**, 150918.
46 S. Shao, S. Xing, K. Bi, T. Zhao, H. Wang, Y. Tang, J. Liu and F. Wang, *Chem. Eng. J.*, 2024, **494**, 152976.
47 A. Rajan, S. K. Solaman and S. Ganesanpotti, *ACS Appl. Mater. Interfaces*, 2023, **15**, 5822–5835.
48 A. Rajan, S. K. Solaman and S. Ganesanpotti, *Adv. Compos. Hybrid Mater.*, 2025, **8**, 203.